Journal of Glaciology



Article

Cite this article: Pohle A, Werder MA, Gräff D, Farinotti D (2022). Characterising englacial R-channels using artificial moulins. *Journal of Glaciology* **68**(271), 879–890. https://doi.org/10.1017/jog.2022.4

Received: 22 May 2021
Revised: 17 January 2022
Accepted: 18 January 2022
First published online: 14 March 2022

Key words:
Glacier discharge; glacier hydrology; glaciological instruments and methods

Author for correspondence:
Annegret Pohle,
E-mail: apohle@ethz.ch

© The Author(s), 2022. Published by Cambridge University Press. This is an Open Access article, distributed under the terms of the Creative Commons Attribution licence (https://creativecommons.org/licenses/by/4.0/), which permits unrestricted re-use, distribution, and reproduction in any medium, provided the original work is properly cited.

cambridge.org/jog

Characterising englacial R-channels using artificial moulins

Annegret Pohle[1,2], Mauro A. Werder[1,2], Dominik Gräff[1,2] and Daniel Farinotti[1,2]

[1]Laboratory of Hydraulics, Hydrology and Glaciology (VAW), ETH Zurich, Zurich, Switzerland and [2]Swiss Federal Institute for Forest, Snow and Landscape Research (WSL), Birmensdorf, Switzerland

Abstract

The englacial and subglacial drainage systems exert key controls on glacier dynamics. However, due to their inaccessibility, they are still only poorly understood and more detailed observations are important, particularly to validate and tune physical models describing their dynamics. By creating artificial glacier moulins – boreholes connected to the subglacial drainage system and supplied with water from surface streams – we present a novel method to monitor the evolution of an englacial hydrological system with high temporal resolution. Here, we use artificial moulins as representations for vertical, pressurised, englacial R-channels. From tracer and pressure measurements, we derive time series of the hydraulic gradient, discharge, flow speed and channel cross-sectional area. Using these, we compute the Darcy–Weisbach friction factor, obtaining values which increase from 0.1 to 13 within five days of channel evolution. Furthermore, we simulate the growth of the cross-sectional area using different temperature gradients. The comparison to our measurements largely supports the common assumption that the temperature follows the pressure melting point. The deviations from this behaviour are analysed using various heat transfer parameterisations to assess their applicability. Finally, we discuss how artificial moulins could be combined with glacier-wide tracer experiments to constrain parameters of subglacial drainage more precisely.

Introduction

The experimental study of englacial and subglacial hydrological systems is inherently challenging due to the difficulty of accessing such systems. Various field techniques have been applied, including (1) water-level measurements, as a proxy for subglacial water pressure, in boreholes (e.g. Fountain, 1994; Hubbard and others, 1995; Harper and others, 2002) and moulins (e.g. Iken, 1972; Andrews and others, 2014; Covington and others, 2020), (2) tracer experiments between multiple boreholes, moulins or the glacier outlet to infer, for instance, discharges, transit velocities and dispersion coefficients (e.g. Sharp and others, 1993; Nienow and others, 1998; Hock and others, 1999; Schuler and others, 2004; Cowton and others, 2013), (3) direct exploration of moulins (e.g. Holmlund, 1988; Gulley and others, 2014; Mankoff and others, 2017) and (4) imaging through borehole cameras, to determine the structure of englacial drainage systems (e.g. Fountain and others, 2005; Church and others, 2019). Current developments include measurement techniques such as the Cryoegg (Prior-Jones and others, 2021), the Glacsweb wireless probe (Hart and others, 2019) or drifters (Alexander and others, 2020) that can be deployed into glacier streams to take in situ measurements. In addition to these in situ measurement techniques, remote geophysical methods have been used to infer properties of glacier drainage systems by radar and seismic imaging (e.g. Harper and others, 2010; Schroeder and others, 2013; Church and others, 2019, 2021; Egli and others, 2021) or by passively measuring seismic noise (e.g. Dalban Canassy and others, 2016; Gimbert and others, 2016; Röösli and others, 2016; Nanni and others, 2020).

However, with the current understanding of englacial and subglacial drainage systems, physical models that aim at representing these systems still require a number of assumptions and involve poorly constrained model parameters, which motivates field experiments such as the one presented in this study. The validation of such models is difficult since measurements of subglacial water pressure, temperature, discharge and flow speed are usually sparse in space and time. Moreover, these measurements often represent bulk values over large portions of the glacier (e.g. Werder and others, 2010). Irarrazaval and others (2021) used one of the most comprehensive sets of observations of a glacier drainage system (Huss and others, 2007) to invert a subglacial drainage model for channel locations and discharge conditions. They found that the available data are insufficient to uniquely constrain the model parameters and that more frequent observations at higher resolution are needed for appropriate constraint. Brinkerhoff and others (2021) arrived at largely the same conclusion as they coupled a subglacial drainage model (Werder and others, 2013) to an ice dynamics model thus enabling the use of surface velocity measurements to invert for subglacial drainage properties.

An example for the lack of experimental model validation is the concept of R-channels (Röthlisberger, 1972), (semi)circular, ice-incised, pressurised conduits that are opened by melt and closed by viscous ice deformation. For such features, melt is commonly calculated

under the assumption that the water temperature follows the pressure melting point and that the frictional and sensible heat results in instantaneous melting of the ice walls. Since their first mathematical description in Röthlisberger (1972), R-channels have been incorporated into the majority of subglacial drainage models to represent the efficient drainage system (e.g. Flowers, 2015; De Fleurian and others, 2018). However, even after decades of applying the theory, the aforementioned assumptions are yet to be validated and the parameters still need better constraints. The latter is particularly important in terms of the friction factor, which controls frictional energy loss and thus the energy available for melting the surrounding ice by parameterising the hydraulic roughness of the channel.

In this paper, we present a new approach to experimentally assess the properties of an englacial R-channel. By using boreholes connected to the subglacial drainage system and supplying them with water from a glacier surface stream, we create englacial features that route the water from the surface to the glacier bed; we use the term *artificial moulin* to refer to such a feature. The part of an artificial moulin which is below the water level experiences pressurised water flow and is thus an artificial, englacial R-channel, which is the focus of this study. Although the concept of artificial moulins as a field technique is not completely new, it has only been used for piezometric observations of the water level (e.g. Röthlisberger and others, 1979). Here, we combine pressure and temperature measurements with salt dilution gauging to derive the temporal evolution of the channel's hydraulic gradient, discharge, water flow speed and cross-sectional area. This way we are able to examine the hydraulic and thermodynamic properties of a single R-channel in detail. The highly resolved time series of both the hydraulic friction factor and of the cross-sectional area enable us to directly test the basic theory of Röthlisberger (1972). In contrast to a natural moulin with its complex geometry, an artificial moulin enables safe deployment of instruments and thus precise measurements, which in turn allows the calculation of R-channel properties.

Methods

Field site

We conducted our experiment in August 2020 on Rhonegletscher, a valley glacier in the central Swiss Alps covering an area of ~15 km^2 (as of 2019), elevations from 3600 to 2200 m a.s.l. and a length of ~8 km (GLAMOS, 1881–2020). The study site was located in the ablation zone between 2450 and 2500 m a.s.l. where a bedrock overdeepening is present. There the ice is ~200 m thick (Grab and others, 2021) and the ice surface slope is 5° southwards (Fig. 1). In summer, local daily ice melt reaches 0.1 m d^{-1}, supplying meltwater to surface streams (Landmann and others, 2021). The streams relevant for our study site originate from several smaller streams ~700 m up-glacier. When crossing the region of the overdeepening, the streams merge into a few larger ones, with discharges of several hundred litres per second each (Fig. S1). In this region, ice flow is compressional and only a few small surface crevasses are present. Just downstream of the study site, these surface streams enter the glacier via moulins (Fig. 1).

Artificial moulins

We created artificial moulins by drilling boreholes of ~0.1 m diameter with a hot water drill (Iken and others, 1976). The boreholes were placed next to relatively large surface streams and were drilled down to the glacier bed. Boreholes which drained were interpreted as to have connected to the glacier's efficient drainage system and were turned into artificial moulins by diverting the neighbouring surface stream into them. Only one (BH15, Fig. 1) of the five drilled boreholes (BH11–BH15) drained directly after the drill reached the bed. The artificial moulin created from this borehole, named AM15, was used for the experiment during the following two weeks. Meanwhile, we kept monitoring the water level in the other boreholes and eventually turned the one with the largest diurnal water level fluctuations (BH13) into an additional artificial moulin (named AM13).

BH15 was drilled on 7 August 2020 to a depth of 187 m and turned into an artificial moulin on 8 August. For the first two days of the experiment (8 and 9 August) the flow in AM15 was pressurised, indicated by a completely water-filled borehole. During the following days, however, the water level dropped continuously. The limiting factor for supply of water to AM15 was the incision rate of the surface stream's spillway to the moulin. Only about half of the stream's water entered AM15. As our experiment relies on pressurised flow, we tried to maximise the water supply through frequent enlargement of the spillway with a pickaxe. However, starting from 10 August it was not possible anymore to maintain pressurised flow with this method.

BH13 was drilled on 6 August 2020, reaching the bed at a depth of 200 m. While there was no direct drainage, 20 h later the water level had dropped by 42 m. On 20 August, we diverted a stream into it (turning it into AM13, Fig. 2a) but measurable flow was only established during the following night. AM13 was completely water-filled for the entire duration of the experiment between 20 and 21 August.

Instrumentation

The instrumentation in each artificial moulin consisted of two Keller DCX-22-CTD loggers measuring electrical conductivity, temperature and pressure. We refer to these loggers as CTDs. The instrumental uncertainty of conductivity was ±5 µS cm^{-1} (microsiemens per centimetre) and the one of temperature ± 0.05 °C. The pressure sensors of the two loggers measured with an uncertainty of ±490 and ±1470 Pa, proportional to their full scale range of up to 100 and 300 m water head, respecively. Each day, we attached the two CTDs at different positions on a static rope and installed them in the artificial moulin such that the lower sensor, which was attached to the end of the rope, was located at least 10 m above the glacier bed, i.e. at ~170 m depth for AM15 and at ~190 m depth for AM13. Once installed, we did not change the setup during one day of measurements. The weight of the sensors and the downward water flow ensured that the sensors' positions were stable. The general setup is shown in Figure 2b and a list of the sensor depths on individual days in the Supplementary material (Table S1). We always used the same two loggers and never changed their relative position.

The rope itself served as a depth and sensor distance measure. Its length was measured under tension typical of that experienced during deployments and we estimate the uncertainty of the sensor distance to be ±1 m. The sensors were lowered by hand into the artificial moulin in the morning and retrieved in the evening on a daily basis, which was necessary to download the recorded data and reset the loggers for the next day. We used a 1 s sampling interval to allow for ~8 h of recording time per deployment.

Our individual tracer experiments characterise the section of the artificial moulin between the two sensors. We call this section the *test-section*. Under the constraint that both sensors had to be submerged, the length of this section was chosen as large as possible (up to 100 m) in order to minimise uncertainties per unit length. This constraint was the reason to reduce the length of the test-section in AM15: six days after activation (14 August), the water level had dropped to 130 m below the surface at midday, when the water supply reaches its daily maximum. As a

https://doi.org/10.1017/jog.2022.4 Published online by Cambridge University Press

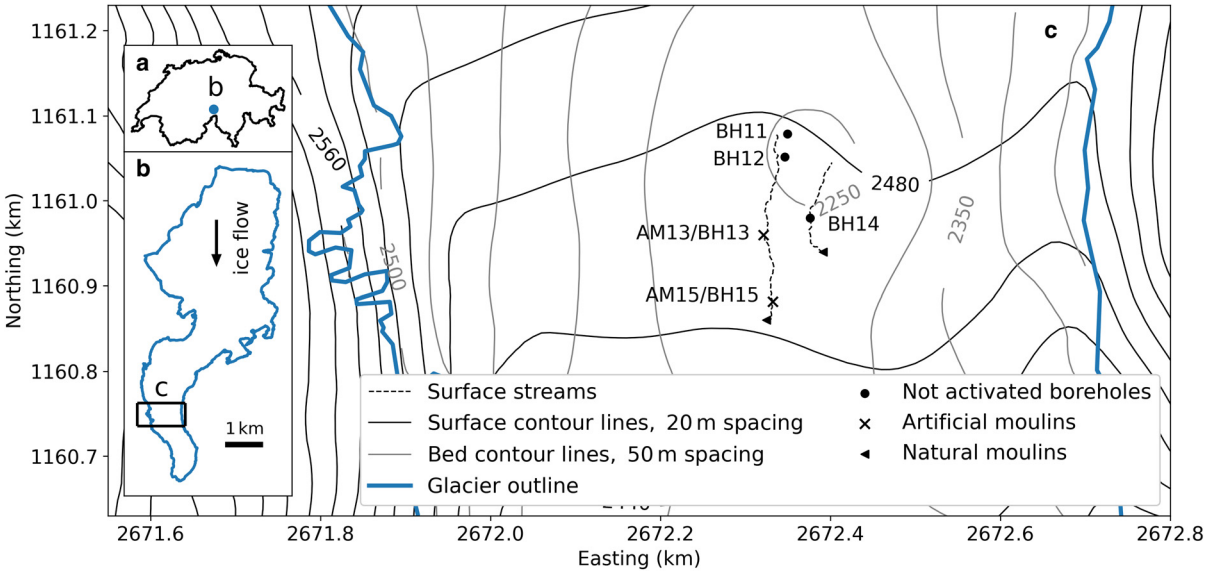


Fig. 1. (a) Location of Rhonegletscher (blue dot) within the borders of Switzerland (black); (b) outline of Rhonegletscher (blue) and indication of study site (black rectangle); (c) map of the study site indicated in (b), including positions of all boreholes and artificial/natural moulins, the closest surface streams, surface and bed topography as well as the glacier outline. The glacier outline in (b) and (c) refers to the state 2016 (Linsbauer and others, 2021). Coordinates are given in the CH1903+/LV95 coordinate system. Figure S1 provides an aerial image of the site.

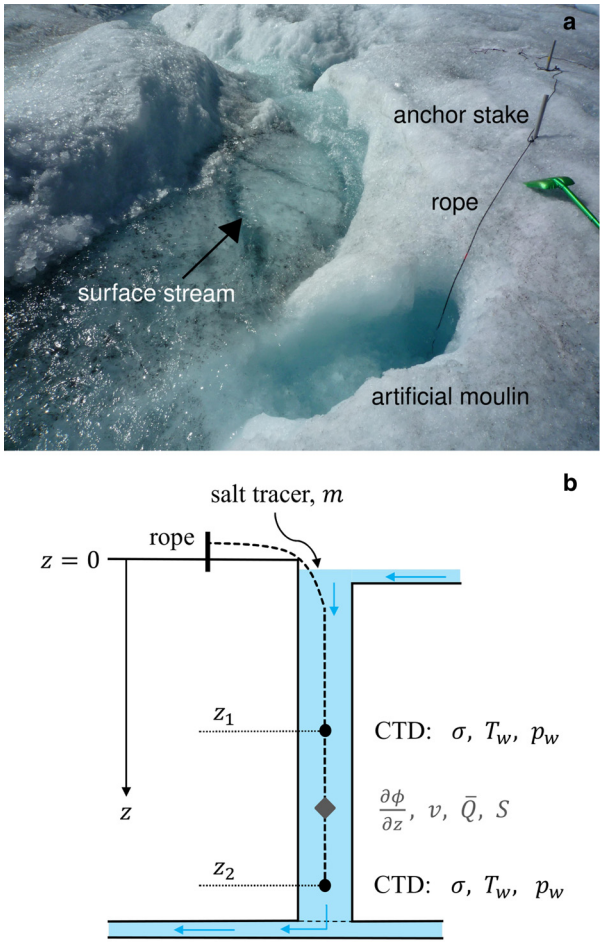


Fig. 2. (a) Artificial moulin AM13 (diameter ~0.2 m) and the feeding surface stream. The rope carrying the conductivity-temperature-pressure sensors (CTDs) is attached to stakes drilled into the ice. The green shovel on the right side of the picture is ~1 m long, for a measure of scale. (b) Schematic setup of the experiment. Two CTDs are installed at two different depths, z_1 and z_2, which span a test-section of varying length (between 30 and 100 m, see Table S1) and measure conductivity σ, water temperature T_w and water pressure p_w. We use these measurements to derive the hydraulic gradient $\partial\phi/\partial z$, flow speed v, mean discharge $\bar{Q}$ and cross-sectional area S as averages over the test-section.

consequence, the upper sensor (at 127 m depth) was left out of the water during the entire day. Eleven days after activation (19 August) the flow was only pressurised to less than 20 m above the lower sensor.

Experimental setup

In this study, artificial moulins represent pressurised englacial R-channels rather than moulins themselves. To investigate the properties of such an R-channel, we use the pressure and depth measurements to infer the hydraulic potential gradient and salt tracer experiments to obtain the discharge and the flow speed. Using these quantities we derive the rest of the hydraulic properties as listed in Table 1.

Water flow in an R-channel (and in general) is driven by the gradient of the hydraulic potential, or hydraulic gradient for short. Neglecting the kinetic potential, the hydraulic potential is given by the sum of elevation potential and water pressure

$$\phi = \rho_w g h + p_w, \tag{1}$$

where ρ_w is the density of water, g the gravitational acceleration, h the elevation relative to a reference point and p_w the water pressure. We neglect the kinetic potential as it is commonly done in glaciology (e.g. Röthlisberger, 1972) and since its gradient is more than an order of magnitude smaller than that of the other components (see Supplementary material). A summary of all physical constants used in this study is given in Table 2 and the symbols and units for physical quantities are listed in Table 1. In our experiment, measuring water pressures at the two sensors with known depths enables us to calculate the hydraulic gradient along the flow direction of the test-section. Since we constructed the experiment to produce purely vertical flow, we can write the hydraulic gradient as

$$\frac{\partial \phi}{\partial z} = \frac{\partial p_w}{\partial z} - \rho_w g \approx \frac{\Delta p_w}{\ell} - \rho_w g, \tag{2}$$

where z is the depth coordinate pointing downwards (in our case along flow), Δp_w the pressure difference and ℓ the length of the test-section. When deriving other quantities from the so-computed hydraulic gradient, we use the pressure averaged over

https://doi.org/10.1017/jog.2022.4 Published online by Cambridge University Press

Table 1. Quantities measured and derived through the experiment. The two uncertainties for the water pressure correspond to the upper and lower CTD sensor, respectively.

Quantity	Symbol	Unit	Uncertainty
Measured			
Water pressure	p_w	Pa	±490, ±1470
Length of test-section	ℓ	m	±0.5
Tracer mass	m	kg	$\pm 2 \times 10^{-3}$
Conductivity	σ	µS cm^{-1}	±5
Water temperature	T_w	°C	±0.05
Derived			
Hydraulic potential	ϕ	Pa	
Salt concentration	c	kg m^{-3}	
Discharge at the sensors	Q	m^3 s^{-1}	
Mean discharge	$\overline{Q}$	m^3 s^{-1}	
Flow speed	v	m s^{-1}	
Cross-sectional area	S	m^2	
Darcy–Weisbach friction	f		
Manning roughness	n'	s m$^{-1/3}$	
Nusselt number	Nu		
Reynolds number	Re		
Equilibrium offset-temp.	τ_{eq}	°C	
Equilibrating length scale	z_{eq}	m	

Table 2. Physical constants used for deriving relevant quantities (listed in Table 1, Eqns (1–8)), running the size evolution models (Eqns (9) and (10)) and calculating the heat transfer parameters (Eqns (11–16))

Constant	Symbol	Value	Unit
Gravitational acceleration	g	9.81	m s^{-2}
Density of water	ρ_w	1 000	kg m^{-3}
Density of ice	ρ_i	910	kg m^{-3}
Latent heat of fusion	L	3.34×10^5	J kg^{-1}
Heat capacity of water	c_w	4 217.7	J kg^{-1} K^{-1}
Thermal conductivity of water	k	0.57	Wm^{-1} K^{-1}
Pressure melt coefficient	c_t		
Pure water	$c_{t\,(pure)}$	-7.4×10^{-8}	K Pa^{-1}
Air saturated water	$c_{t\,(air)}$	-9.8×10^{-8}	K Pa^{-1}
Dynamic viscosity of water	μ_w	1.787×10^{-3}	Pa s
Prandtl number	Pr	13.5	

a time period which starts when the tracer is first visible in the readings of the upper sensors and ends when it ceases to be visible in the readings of the lower sensor. This duration is mostly ∼2–3 min in AM15 and between 20 and 30 min in AM13 where the velocities and discharges are smaller and the test-section is longer.

The discharge and the water flow speed are obtained by salt dilution gauging using measurements of electrical conductivity. In the field, we performed discrete injections of NaCl with a known mass, typically 25–100 g, at time intervals spanning from 20 min to a few hours. The mass was measured with an analogue suspended scale, and we estimated the uncertainty to 2 g by repeated comparisons with a digital kitchen scale. Before injecting the salt, we dissolved it in ∼1 L of water. For a well-mixed salt tracer in a confined channel, the injection mass m is equal to the time integral of discharge Q times the salt concentration c. Assuming that the discharge is constant over the course of a tracer signal, one can write

$$m = Q \int_{t_0}^{t_1} c(t)\,\mathrm{d}t, \tag{3}$$

with the integration interval $[t_0,\ t_1]$ over the time span during which the concentration is above the background level. The salt concentration $c(t)$ is proportional to electrical conductivity $\sigma(t)$, and the factor of proportionality is determined from four calibrations conducted in the field. In each calibration, we measured the conductivity at different known salt concentrations, which is used to fit a linear function $c = a\,\sigma$ with a proportionality factor a for each sensor. The time series of $c(t)$ in the individual tracer experiments further allow the calculation of the average flow speed v, for which we use

$$v = \frac{\ell}{\Delta t_{c_{max}}}, \tag{4}$$

with $\Delta t_{c_{max}}$ being the time difference between the peak concentrations at the two sensors. Finally, the test-section's average cross-sectional area S is obtained with

$$S = \overline{Q}/v, \tag{5}$$

where $\overline{Q}$ is the mean value between the discharges at the two sensors. Note that we only conduct this calculation when the discharges at the two sensors agree within their uncertainties. Finally, the Reynolds number, a measure of turbulence, is given by

$$\mathrm{Re} = 2|v|\sqrt{\frac{S}{\pi}}\frac{\rho_w}{\mu_w}, \tag{6}$$

with μ_w being the dynamic viscosity of water.

Propagation of uncertainties

For the forward propagation of measurement uncertainties we use a Monte Carlo approach: quantities with uncertainties are represented with ensembles of 20 000 samples each from Gaussian distributions with standard deviations equal to the given or estimated uncertainties (Table 1). All calculations are then carried out with these ensembles, in turn yielding ensembles of results with the corresponding statistical distributions. These Monte Carlo uncertainty calculations are carried out using the software package MonteCarloMeasurements.jl (Bagge Carlson, 2020). Note that we treat the stated instrumental uncertainties (Table 1) as systematic and thus the mean of repeated measurements does not have a reduced uncertainty. The uncertainties of the derived quantities are stated as the standard deviations of the resulting distributions and are plotted with error bars in Figures 3–5.

Friction factor

Discharge and flow speed are related to the hydraulic gradient, which is commonly captured in terms of the empirical Darcy–Weisbach equation (Weisbach, 1845). In the case of a circular, vertical conduit it reads

$$\frac{\partial \phi}{\partial z} = f\frac{\rho_w}{4}\sqrt{\frac{\pi v^5}{Q}}, \tag{7}$$

where f is the Darcy–Weisbach friction factor, which can be understood as an effective factor absorbing any effects of non-circular conduits. However, in our setup we do not expect major deviations from the circular cross-section since the conduits of interest are both pressurised and vertical, which prevents local incision, and since we conducted the experiment within one week after drilling, a timescale where viscous ice deformation should be of minor importance. Since we measure and derive all remaining quantities, we can compute f directly. To do so, we use the spatial discretisation from Eqn (2) for $\partial\phi/\partial z$ and take $\overline{Q}$ for the discharge. Thus the derived friction factor is also an average value over the test-section. The calculation of f through Eqn (7) is only applicable when the flow is pressurised rather than a waterfall.

In order to facilitate comparisons with other studies, we also compute the Manning roughness n', which is often used as an

https://doi.org/10.1017/jog.2022.4 Published online by Cambridge University Press

alternative way to relate the hydraulic potential to discharge. For a circular channel, the conversion between f and n' is (e.g. Clarke, 2003)

$$n' = \left(\frac{S}{4\pi}\right)^{1/12}\sqrt{\frac{f}{8g}}. \tag{8}$$

Model for channel size evolution

According to Röthlisberger (1972), R-channels are opened through melting the ice walls. In Röthlisberger's formulation, the amount of melt is obtained from considerations of energy balance, where the energy for melt is provided both by frictional dissipation and by sensible heat changes due to the water temperature changing along the channel. In the majority of subglacial drainage models, the temperature is assumed to be at a constant offset from the pressure-dependent melting point (Flowers, 2015). Under this assumption, the temperature gradient is equal to the gradient of the pressure melting point and obtained directly from multiplying the pressure gradient with the pressure melt coefficient c_t. The fact that this approach avoids solving for the water temperature as a field variable makes it numerically cheap and attractive to apply.

In order to test this assumption, we simulate the size evolution of our test-sections with two different models. In the simpler one, we follow the aforementioned assumption, therefore fixing the temperature gradient at the melting point gradient (referred to as the c_t-*gradient model*), and in the second model we perform a Bayesian inversion with the temperature gradient as a parameter that we fit to the experimental data of the cross-sectional area (the *free-gradient model*). The latter allows us to determine a confidence interval for the temperature gradient, and we can test whether the temperature gradients predicted by the c_t-gradient model are included within that interval. In both models, we neglect the closure of R-channels through viscous ice deformation since it is insignificant in our case: after calculation it turns out that the largest closure rates are three orders of magnitude smaller than the opening rates (Table S3, Figs S3 and S4).

In the c_t-gradient model, the evolution of the cross-sectional area is described through

$$\frac{\partial S}{\partial t} = -\frac{Q}{\rho_i L}\left(\frac{\partial \phi}{\partial z} + c_w \rho_w c_t \frac{\partial p_w}{\partial z}\right), \tag{9}$$

where ρ_i is the ice density, L the latent heat of fusion and c_w the heat capacity of water. The first term, proportional to $\partial\phi/\partial z$, describes frictional heat dissipation while the second one, proportional to the melting point gradient $c_t \partial p_w/\partial z$, is related to the sensible heat. Here, we take c_t as negative, noting that it is also common to define it as positive (e.g. Clarke, 2003). Since c_t depends on the air saturation of the water, its value is not accurately constrained. Two values are typically used: for pure water $c_{t\,(\mathrm{pure})} = -7.4 \times 10^{-8}\ \mathrm{K\,Pa^{-1}}$ and for air saturated water $c_{t\,(\mathrm{air})} = -9.8 \times 10^{-8}\ \mathrm{K\,Pa^{-1}}$ (Harrison, 1975). We forward-propagate uncertainties through the c_t-gradient model by assuming that the c_t values are uniformly distributed over the interval $[c_{t\,(\mathrm{air})},\ c_{t\,(\mathrm{pure})}]$ and by using the above-determined uncertainties for Q, $\partial\phi/\partial z$, $\partial p_w/\partial z$ and the initial S. Both models predict the evolution of S over the time period of tracer experiments on a single day, therefore the initial condition describes the state when the first tracer was injected on the corresponding day.

For the free-gradient model, we replace the melting point gradient in Eqn (9) by a general temperature gradient

$$\frac{\partial S}{\partial t} = -\frac{Q}{\rho_i L}\left(\frac{\partial \phi}{\partial z} + c_w \rho_w \frac{\partial T_w}{\partial z}\right), \tag{10}$$

where T_w is the water temperature. Note that more negative water temperature gradients lead to larger opening rates. We fit the evolution of S modelled through Eqn (10) to the experimental data of S by a Bayesian inversion (Bayes, 1958) using $\partial T_w/\partial z$ and the initial S as the fitting parameters. For the likelihood function, which compares modelled and measured S, we impose a Gaussian distribution on the uncertainties. This is done by assuming independent measurements and by using the measurement uncertainty as the distribution's standard deviation. As a prior for the initial S, we choose a Gaussian distribution around the measurement with its uncertainty as standard deviation. For the prior of $\partial T_w/\partial z$, we impose a uniform distribution which is non-zero only for $\partial T_w/\partial z \in [-10^{-2},\ -10^{-6}]\ \mathrm{K\,m^{-1}}$. (See the Supplementary material, in particular Eqns (S7–S8), for a detailed description of the mentioned priors and likelihoods.) Uncertainties of the input parameters $\overline{Q}$ and $\Delta p_w/\ell$ are neglected as otherwise the number of fitting parameters would increase from 2 to ~30. We run the Bayesian inversion by employing an affine invariant Markov chain Monte Carlo (MCMC) sampler (Goodman and Weare, 2010) with 10^6 iterations via the software package KissMCMC.jl (Werder, 2021). To discretise the spatial derivative in Eqns (9) and (10), we use Eqn (2). For the time stepping we use an explicit forward Euler scheme with the time step equal to the interval between tracer injections (i.e. ~20 min).

Heat transfer

When water flows in a long R-channel under steady conditions, the water temperature approaches an equilibrium temperature T_{eq} (Isenko and others, 2005; Sommers and Rajaram, 2020). In our case, where the channel is vertical and pressurised, T_{eq} changes along the flow due to the depression of the pressure melting point. Here, it is rather the offset of T_{eq} from the melting point that approaches an equilibrium. In the following, we refer to this offset as the *offset-temperature* $\tau = T - T_i$, where T_i is the ice temperature. Note that T can either refer to the water temperature T_w or to the equilibrium temperature T_{eq} with corresponding offset-temperatures τ_w and τ_{eq}, respectively. The ice temperature T_i is assumed to be at the pressure melting point since Rhonegletscher is a temperate glacier.

From the steady-state energy balance along the channel, a water temperature equation can be derived (Eqns (S10–S16)). When stated in terms of the offset-temperatures, it reads

$$z_{eq}\frac{\partial \tau_w}{\partial z} = \tau_{eq} - \tau_w, \tag{11}$$

where

$$\tau_{eq} = -\frac{Q}{\pi k \mathrm{Nu}}\left(\frac{\partial \phi}{\partial z} + \rho_w c_w c_t \frac{\partial p_w}{\partial z}\right), \tag{12}$$

and z_{eq} the equilibrating length scale

$$z_{eq} = \frac{\rho_w c_w Q}{\pi k \mathrm{Nu}}. \tag{13}$$

Here, k is the thermal conductivity of water and Nu the Nusselt number quantifying turbulent heat transfer. Solving Eqn (11) gives

$$\tau_w(z) = \tau_{eq} + (\tau_{w0} - \tau_{eq})\exp\left(\frac{-z}{z_{eq}}\right), \tag{14}$$

where τ_{w0} is the water offset-temperature at $z = 0$.

If we know Nu, we can gain insights into the thermodynamics of the system by using both our measurements and the free-gradient model outputs to derive the thermodynamic variables z_{eq}, τ_{eq} and τ_w. In particular, the free-gradient model allows us

https://doi.org/10.1017/jog.2022.4 Published online by Cambridge University Press

to constrain the temperature gradient $\partial T_w/\partial z$ more accurately than the measurements, thus we use $\partial \tau_w/\partial z = \partial T_w/\partial z - c_t \partial p_w/\partial z$. The Nusselt number Nu is not accurately constrained but can be obtained from hydraulic variables via empirical formulas. Most commonly used is the Dittus–Boelter equation

$$\mathrm{Nu} = A\,\mathrm{Pr}^{\alpha}\mathrm{Re}^{\beta}, \tag{15}$$

where Pr = 13.5 is the Prandtl number and Re is given by Eqn (6). Another formula to obtain Nu is the Gnielinski correlation (Gnielinski, 1975)

$$\mathrm{Nu} = \frac{(f/8)(\mathrm{Re} - 1000)\mathrm{Pr}}{1 + 12.7(f/8)^{1/2}(\mathrm{Pr}^{2/3} - 1)}, \tag{16}$$

which additionally depends on the hydraulic friction factor f. To obtain the thermodynamic variables described above, we calculate Nu with six different parameterisations, summarised in Table 3. Five of them correspond to different sets of coefficients for the Dittus–Boelter equation (Eqn (15)) and the sixth parameterisation is the Gnielinski correlation (Eqn (16)). The parameterisation of Nu depends on the flow regime and thus the different correlations are always associated with certain ranges of Re values, which are also given in Table 3.

First, we use a set of coefficients that has been the standard in glaciology (e.g. Nye, 1976; Spring and Hutter, 1982; Clarke, 2003) even though they were derived for engineering applications with experiments of water flowing through heated pipes. The coefficients of Lunardini and others (1986) were also obtained from laboratory experiments but specifically in an ice-water related setup. In recent years, the Dittus–Boelter coefficients were fitted to glaciological field data (Vincent and others, 2010; Ogier and others, 2021), albeit for surface streams with relatively warm water coming from a lake. Furthermore, we apply a set of coefficients that was proposed by the theoretical study of Sommers and Rajaram (2020) for the case where all heat is generated by frictional dissipation. Finally, we apply the Gnielinski correlation, which is a refinement of the Dittus–Boelter equation with standard coefficients but which has had limited application in glaciology to date (Ancey and others, 2019). For each of these Nu parameterisations, we calculate τ_w using Eqn (11) and compare it to our temperature measurements in order to test whether the different parameterisations for Nu are applicable to our test-section.

Results

Measurements

In the time period 8–21 August 2020, we performed a total of 70 tracer injections in the two artificial moulins AM15 and AM13. After calculation of the discharge, we select 40 tracer experiments suitable for further considerations. The selection is based on two criteria: we require that (1) both sensors are at least 5 m below the water table, recognisable from the pressure record and (2) the discharge estimates at the two sensors are consistent, i.e. overlapping within their uncertainty ranges. In AM15, which we used for the experiment from 8 to 19 August, the limiting factor is the continuously dropping water level (see Fig. S2 and 'Data/code availability' section). In AM13, where the experiment lasted only for two days (20 and 21 August), the selection of only the second day is due to insufficient water flow on the first day.

Selected measured and derived quantities are summarised in Figure 3 (see also Table 1). In AM15 (left panels), discharge and flow speed measurements of 9 and 11 August capture daily variations, with peak values in the early afternoon. The flow speed decreases over the six day measurement period, whereas the discharge and the hydraulic gradient do not show a recognisable trend. Consequently, the cross-sectional area increases over time, with a clear linear trend on 9 August. Note that the inflow into AM15, and therefore the melt enlargement, was stopped during the nights from 8 to 9 and 9 to 10 August. In AM13 (right panels of Fig. 3), the absolute hydraulic gradient is low throughout the single day of measurements. Accordingly, the discharges, velocities and the opening rate of the cross-sectional area are much smaller than in AM15. The friction factor f fluctuates between 0.1 and 0.4 on 8, 9 August (AM15) and 21 August (AM13), corresponding to n' between 0.02 and 0.04 $\mathrm{s\,m^{-1/3}}$. In AM15, the friction increases from 10 August onwards to reach a maximum of $f = 13$ on 13 August.

Observed and modelled size evolution

To compare the modelled opening rates to the measurements, we focus on the two days with the most dense measurements, i.e. 9 and 21 August 2020 (using AM15 and AM13, respectively); we will refer to them as *9-Aug/AM15* and *21-Aug/AM13*, respectively. On both days, the size evolution inferred from the c_t-gradient model overlaps with the measurements (Fig. 4) meaning that the c_t-gradient model is in principle successful at predicting the evolution of the cross-sectional area. However, the prediction of the free-gradient model follows the measurements more accurately.

Figures 4c, d show the temperature gradients corresponding to the c_t-gradient model, the free-gradient model and the measurements. We compare the posterior distribution of $\partial T_w/\partial z$ of the free-gradient model to the temperature gradient distributions both calculated from temperature measurements and predicted by the c_t-gradient model. The observed temperature gradients agree with both models' results, but the measurement uncertainties are too large to make any further statements about the question whether the temperature gradient follows the depression of the pressure melting point. For 9-Aug/AM15, the uncertainty is notably larger since the length of the test-section ℓ is only 50.6 m (compared to 101.5 m for 21-Aug/AM13). With a test-section of ~100 m, achieving an observational accuracy comparable to the model results would require measurement uncertainties of absolute temperature smaller than ~0.002 °C.

The temperature gradient of the c_t-gradient model (the melting point gradient) overlaps with the 95% confidence interval of the posterior from the free-gradient model inversions on both days, meaning that the c_t-gradient model is able to explain the derived S time series for each day individually. However, the overlaps are only small and on opposite ends of the c_t range for the two days: for 9-Aug/AM15, only the models with c_t values close to the lower limit $c_{t\,(\mathrm{pure})}$ (smaller absolute gradient) lie within the confidence interval, whereas for 21-Aug/AM13 only the values close to the upper limit at $c_{t\,(\mathrm{air})}$ lie therein. Since there is no indication for the c_t values being different between the two days, it follows that the c_t-gradient model is not able to explain the time series of both days *simultaneously*. This means that the actual water temperature gradients are different from the ones predicted by the c_t-gradient model.

The models can also be used to calculate the relative contributions of frictional dissipation and sensible heat change to ice melt. The c_t-gradient model predicts that averaged over the day, sensible heat provides 66 ± 7% of the total energy for 9-Aug/AM15 and 90 ± 11% for 21-Aug/AM13, when the discharges and hydraulic gradients are smaller. In the free-gradient model, the contribution of sensible heat is 57 ± 4% for 9-Aug/AM15 (smaller than in the c_t-gradient model) and 94 ± 6% for 21-Aug/AM13 (larger than in the c_t-gradient model). Compared to the free-gradient model, the c_t-gradient model predicts total melt rates that are on average 26 ± 9% larger for 9-Aug/AM15 and 40 ± 6% smaller for

https://doi.org/10.1017/jog.2022.4 Published online by Cambridge University Press

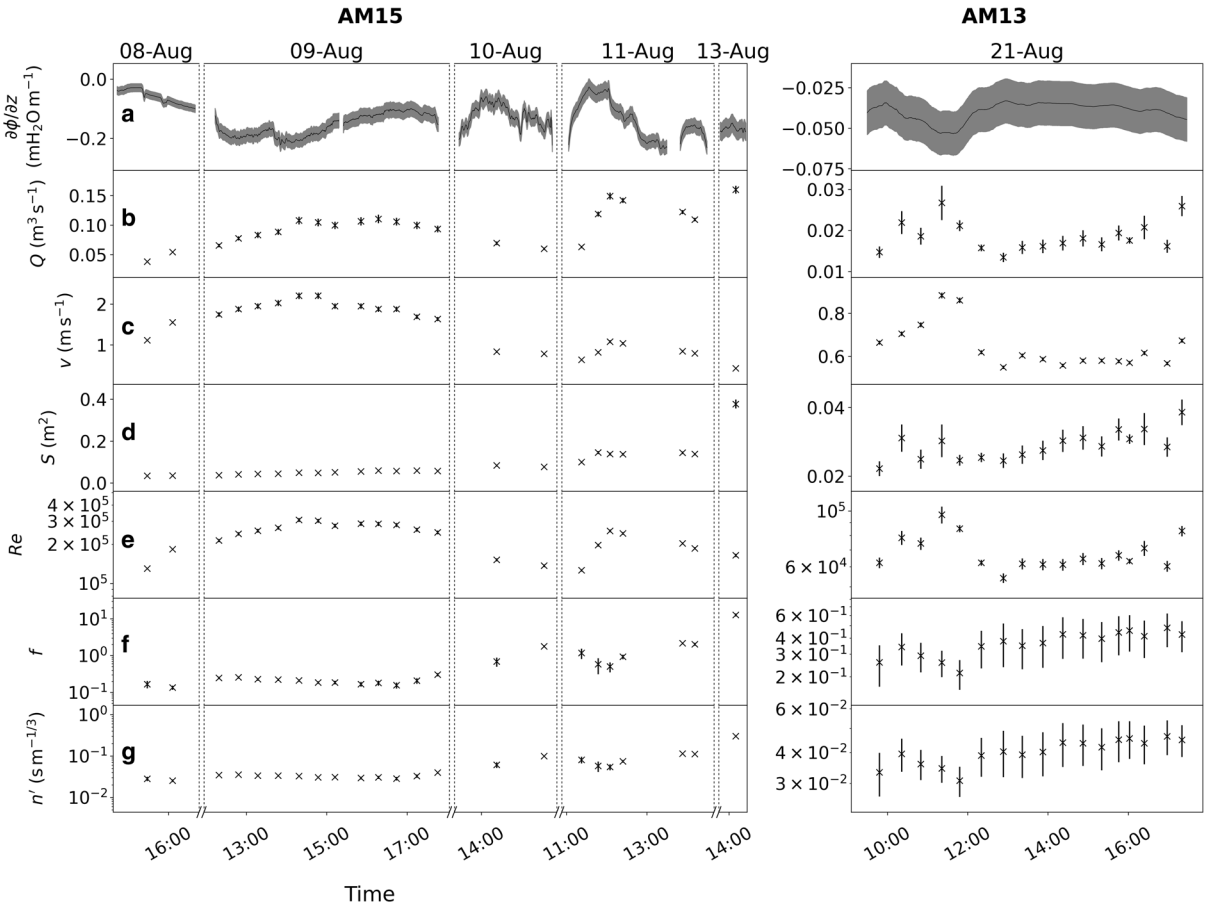


Fig. 3. Quantities derived for the test-section of the investigated artificial moulins (AM) (corresponding to Eqns (2–8)). The following quantities are shown: (a) hydraulic gradient $\partial\phi/\partial z$, smoothed with a moving average filter with window of size ±1 min (AM15) and ±15 min (AM13), which is the typical duration during which the tracer is visible; (b) discharge Q; (c) flow speed v; (d) cross-sectional area S; (e) Reynolds number Re; (f) Darcy–Weisbach friction factor f and (g) Manning roughness n'. Note that the scale of the y-axis differs between AM15 (left) and AM13 (right) and that measurements of the hydraulic gradient are logged continuously while the other quantities rely on manual tracer injections. For the hydraulic gradient, we only show measurements where the flow between the two sensors is pressurised. Uncertainties are given as one standard deviation and are represented by either a grey area (hydraulic gradient) or vertical lines (other quantities).

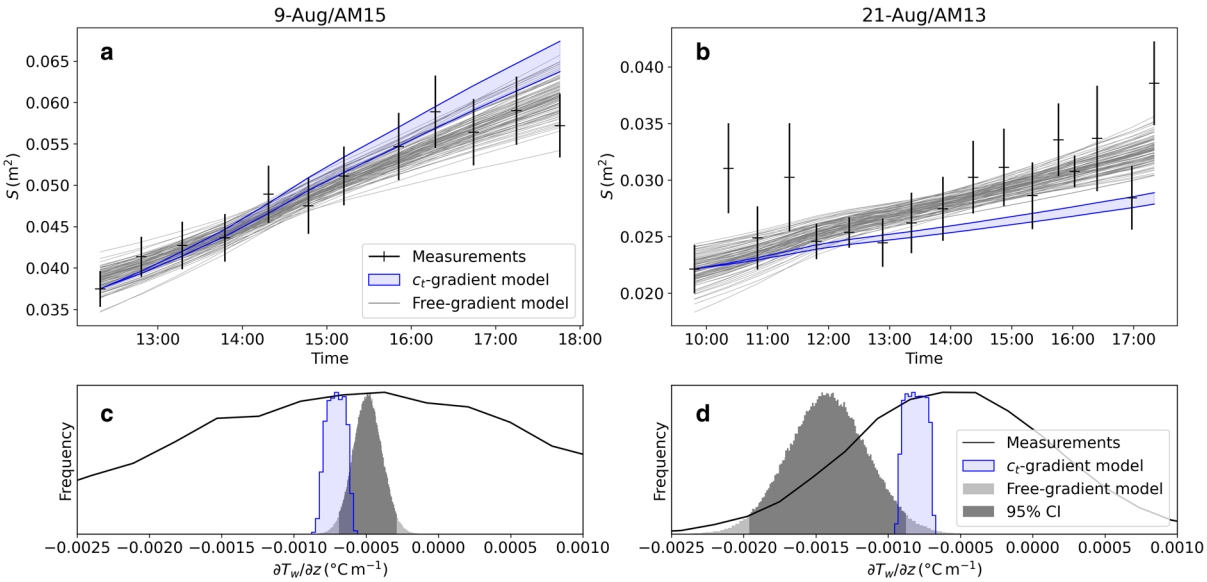


Fig. 4. Size evolution of the cross-sectional area S of artificial moulin (a) AM15 on 9 August 2020 and (b) AM13 on 21 August 2020 as calculated from measurements (black markers with error bars), the c_t-gradient model (blue area) and the free-gradient model (grey lines resulting from some of the individual MCMC iterations fitting $\partial T_w/\partial z$ and the initial S). The lower panels show probability densities for the temperature gradient for 9-Aug/AM15 (c) and 21-Aug/AM13 (d): temporal mean of measured temperature gradient $\overline{\Delta T_w}/\ell$ (black line); temporal mean of melting point gradient as predicted by the c_t-gradient model (blue); posterior distribution of $\partial T_w/\partial z$ inferred by the free-gradient model (grey) with 95% confidence interval (CI) highlighted explicitly (dark grey).

https://doi.org/10.1017/jog.2022.4 Published online by Cambridge University Press

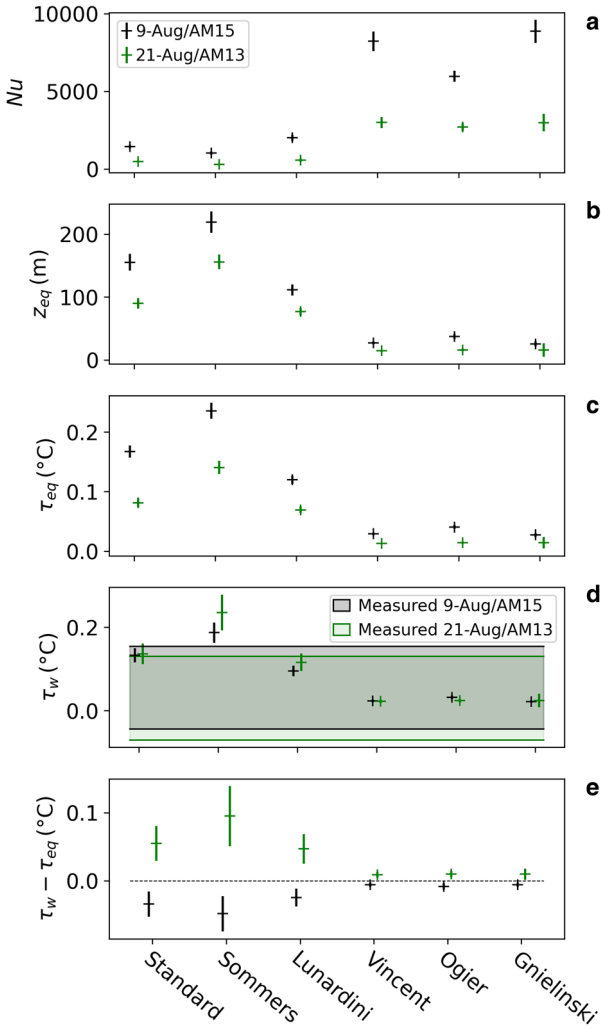


Fig. 5. Daily means of thermodynamic properties, derived from six different Nu parameterisations (Eqns (15) and (16), Table 3): (a) Nusselt number Nu, (b) equilibrating length scale z_{eq}, (c) equilibrium offset-temperature τ_{eq}, (d) water offset-temperature τ_w and (e) difference between water offset-temperature and equilibrium offset-temperature. Panel (d) also shows the 95% confidence interval of the τ_w measurements. The figure only shows daily mean values because the daily variations are much smaller than the difference between the daily mean values of the Nu parameterisations (see Fig. S6).

21-Aug/AM13. The opening rates of both models and their partitioning are plotted and listed in the Supplementary material (Fig. S3, Table S3).

Heat transfer

Since the heat transfer calculations depend on the results from the size evolution models, we focus on the same days here, 9 August (AM15) and 21 August 2020 (AM13). Figure 5 shows the daily mean values for the thermodynamic variables z_{eq}, τ_{eq} and τ_w, as well as $\tau_w - \tau_{eq}$ for the different Nusselt number parameterisations. Note that we treat the different coefficients for the Dittus–Boelter equation as individual parameterisations.

The results can be divided into two groups: a low heat-transfer group, comprising the Dittus–Boelter equation with coefficients either from the standard formula (e.g. Clarke, 2003), from Sommers and Rajaram (2020) or from Lunardini and others (1986), and a high heat-transfer group comprising the Dittus–Boelter equation with coefficients from Vincent and others (2010) or Ogier and others (2021), or the Gnielinski correlation (Gnielinski, 1975). The low-heat transfer group shows lower Nu, longer equilibrating length scales z_{eq}, higher equilibrium offset-temperature τ_{eq} and higher water offset-temperature τ_w than the latter group, and vice versa. The discrepancy between the two groups is large: for example, τ_w is ~0.12 °C for the former and ~0.02 °C for the latter. Note that the close correspondence of the results within each of the two groups are particular to our setting and that the grouping would break apart at much higher or lower Reynolds numbers (the parameterisations depend on this number with an exponent varying from 0.58 to 1).

Table 3. Parameterisations used to calculate Nu and the range of Re values for which they were determined. For the ones based on the Dittus–Boelter equation (Eqn (15)), dimensionless coefficients A, α and β are given. The different parameterisations are categorised into low and high heat-transfer, corresponding to low and high Nu values, respectively, for the conditions encountered in this study.

Study	*A*	α	β	Re range
Low heat-transfer				
Standard (e.g. Clarke, 2003)	0.023	2/5	0.8	$2\,500 < Re < 2.4 \times 10^5$
Sommers and Rajaram (2020)	0.0025	2/5	0.95	$10^4 < Re < 10^6$
Lunardini and others (1986)	0.0078	1/3	0.927	$2 \times 10^4 < Re$
High heat-transfer				
Vincent and others (2010)	0.332	1/3	0.74	Not stated
Ogier and others (2021)	1.78	1/3	0.58	$5 \times 10^5 < Re < 2 \times 10^6$
Gnielinski (1975)	Not applicable			$2\,300 < Re < 10^6$

The Reynolds numbers that we obtain are between 6×10^4 and 3×10^5 (Fig. 3) and thus mostly in the ranges over which the Nu correlations are stated to be valid (Table 3). The only exception is the correlation of Ogier and others (2021), but their Re range only represents the conditions under which the experiments were conducted and therefore the validity is not necessarily exclusive to this range.

Between 9-Aug/AM15 and 21-Aug/AM13, all parameterisations show the same differences for all thermodynamic variables except for τ_w. For instance, all parameterisations predict a lower τ_{eq} for 21-Aug/AM13 than for 9-Aug/AM15. In terms of the difference between τ_w and τ_{eq} (Fig. 5e) all parameterisations predict a water offset-temperature above the equilibrium offset-temperature for 9-Aug/AM15 and below the equilibrium offset-temperature for 21-Aug/AM13. Comparing the measured τ_w with values from the different Nu parameterisations (Fig. 5d) shows that all parameterisation are able to explain the measurements to within the 95% confidence interval except for the one by Sommers and Rajaram (2020).

Discussion

The results show that artificial moulins can provide insights into the hydraulics and evolution of an englacial R-channel. To our knowledge, the time series that we derive for hydraulic gradient, discharge, flow speed and cross-sectional area are the first of their kind.

Friction factor

Within the first two days after activation of the artificial moulins, the derived Darcy–Weisbach friction factor lies between 0.1 and 0.5. This is well within the range of values that are typically used in modelling studies, between 0.01 and 0.5 (e.g. Clarke, 2003; Werder and others, 2013). However, between 10 and 13 August the friction factor determined for AM15 increases considerably, reaching a value of 13. A possible explanation for this increase could be the development of scallops, periodic cavities eroded into the ice, which have been shown to form spontaneously when a flat ice surface is in contact with flowing water and which can reach a steady-state geometry (e.g. Bushuk and

https://doi.org/10.1017/jog.2022.4 Published online by Cambridge University Press

others, 2019). To further investigate the evolution of the friction factor, in particular to determine whether it eventually reaches a steady value, it would be necessary to carry out measurements over a longer time period. This would require a site with higher subglacial water pressure to keep the flow in the artificial moulin pressurised such that it continues to operate as an englacial R-channel.

However, even if such a steady-state was reached, the artificial moulin would still differ from an R-channel that has formed by itself. The main difference would likely be the shape, as natural R-channels are not perfectly straight and can have wide and flat cross-sections (Hooke and others, 1990; Church and others, 2019). In particular the sinuosity can have a major impact on the friction factor, at least in the case of subglacial conduits (Chen and others, 2018). Both an elliptic cross-section and sinuosity would increase the friction, thus the values we derive for the friction factor likely represent lower bounds. Note that the inclination of the channel does not play a role as long as the flow is pressurised, and thus our results are transferable to horizontal channels.

The comparison to subglacial channels is difficult since the contact to the bed adds complexity and also a dependence on the type of the glacier bed. Chen and others (2018) derived friction factors of up to 2.34 for a pressurised channel with sediment bed and ice roof, whereas Gulley and others (2014) reported friction factors of up to 75 (for open channel flow conditions). The comparison to our results emphasises that a single friction factor, constant in space and time, cannot be effectively used to parameterise the dissipation of energy in both englacial and subglacial systems.

Comparison of size evolution models

The time series of the hydraulic variables in the test-sections allows us to test the most commonly used size evolution model, where the temperature gradient $\partial T_w/\partial z$ is fixed at the melting-point gradient $c_t \partial p_w/\partial z$ (the c_t-gradient model). To this end, we compare the c_t-gradient model to the free-gradient model, which uses $\partial T_w/\partial z$ as a parameter to fit the observed channel opening rates (note that the potential energy dissipation term is identical in both models).

The opening rates of the c_t-gradient model differ by $\sim$35% from the opening rates of the free-gradient model (cf. Table S3). When conducting a glacier-wide modelling study, employing a more advanced model including temperature as a field variable (e.g. Nye, 1976; Spring and Hutter, 1982; Clarke, 2003) would be physically more correct, but we suspect that the overall uncertainties would dominate any gains of modelling the temperature explicitly. In general, a model like the c_t-gradient model is accurate for situations similar to our field experiment, i.e. where the R-channel is at a roughly constant angle, the water temperature is already close to the equilibrium temperature when entering the channel and the equilibrating length scale z_{eq} is small compared to the domain of interest.

In other scenarios, for example for lake drainages involving relatively warm (say 2 °C) water, the temperature gradients will differ significantly from the melting point gradient over several equilibrating length scales (Eqn (13)) and thus provide a considerable amount of sensible heat that is not accounted for in the c_t-gradient model. In these situations, modelling the water temperature explicitly is indispensable (e.g. Clarke, 2003). Slightly different conditions arise in the case of channels along adverse slopes, where the pressure melting point increases along flow, reducing the amount of energy available for melting. As a consequence, τ_{eq} is smaller (see Eqn (12)), becomes zero when the adverse slope reaches the supercooling threshold (e.g. Hooke, 1991; Alley and others, 2003; Werder, 2016) and will be negative beyond that threshold. Indeed, beyond the threshold the only available energy for water warming and wall melting is the heat advected by the water. If that heat is not sufficient, refreezing and thus channel shutdown will occur. Modelling such a scenario will benefit from an explicit treatment of the temperature if the lengths of the adverse slopes are comparable to or smaller than the equilibrating length scale; this would, for instance, allow the model to capture channels existing on short, adverse slopes beyond the supercooling threshold.

Heat transfer

Using the thermodynamic variables z_{eq}, τ_{eq} and τ_w, we try to explain why the fitted temperature gradients are smaller than the melting point gradient for 9-Aug/AM15 and larger for 21-Aug/AM13. Theoretically, Eqn (14) predicts that the water offset-temperature τ_w approaches the equilibrium offset-temperature τ_{eq} exponentially. For 9-Aug/AM15, τ_w must be approaching τ_{eq} from lower temperatures, as $c_t \partial p_w/\partial z < \partial T_w/\partial z$ (Fig. 4c) means that τ_w is increasing, and vice versa from higher temperatures for 21-Aug/AM13 (Fig. 4d). This is consistent with the result that irrespective of the Nu parameterisation used, $\tau_w < \tau_{eq}$ for 9-Aug/AM15 and $\tau_w > \tau_{eq}$ for 21-Aug/AM13 (Fig. 5e). However, we cannot confirm this with direct observations due to the large uncertainties in τ_w (compare Figs 5c, d). The question is now whether the discrepancy is due to the two days and sites having different τ_w, τ_{eq} or both.

The heat transfer calculations (Figs 5c–e) show that, irrespective of the used Nu parameterisation, the equilibrium offset-temperature τ_{eq} is higher for 9-Aug/AM15 than for 21-Aug/AM13, while τ_w is very similar on both days (for each Nu-parameterisation, τ_w is in-between the τ_{eq} values of 9-Aug/AM15 and 21-Aug/AM13). This suggests that the discrepancy in the fitted temperature gradients is due to a difference in τ_{eq} between the two days and sites, rather than due to a difference in temperature at the entry of the test-section. To answer why τ_{eq} is different between the two days and sites, we turn to Eqn (12) which shows that τ_{eq} is proportional to the ratio between the opening rate predicted by the c_t-gradient model (see Eqn (9)) and Nu. Both the c_t-gradient model opening rate and Nu are larger for 9-Aug/AM15 than for 21-Aug/AM13. However, the opening rate is about six times larger for 9-Aug/AM15 (see Supplementary material, Table S3) while Nu is only about three times larger (Fig. 5a). Thus, τ_{eq} is larger for 9-Aug/AM15 than it is for 21-Aug/AM13. The interpretation that the test-section entry temperature is similar on both days and sites is in line with the observation that the conditions in terms of meteorology (air temperature, cloudiness), topography (surface channel slope and morphology) and flow characteristics (fully pressurised conditions throughout the artificial moulin) were similar between the two days and sites, such that there is no strong indication that the surface water temperature nor the test-section entry temperature should be different between the two days and sites.

To interpret the temperature gradients, we can additionally take the temperature equilibrating length scale z_{eq} into account. Using Eqn (14), we can calculate the required water temperature at the surface entrance of the artificial moulin in order to reach the inferred τ_w at the mean depth of the test-section. Unfortunately, this back-calculation relies on a growing exponential function and thus the uncertainties also grow exponentially. The uncertainties for the high heat-transfer cases (small z_{eq}) are particularly high, precluding any inference on the surface temperatures. For the low heat-transfer cases, the temperature of the water entering the artificial moulin is estimated to be 0.05 ± 0.04 °C (9-Aug/AM15) and 0.35 ± 0.12 °C (21-Aug/AM13), which is plausible. Due to the large uncertainties of the surface temperatures in the high heat-transfer cases, it is not possible to discriminate between the high and low heat-transfer Nusselt number parameterisations.

https://doi.org/10.1017/jog.2022.4 Published online by Cambridge University Press

The second method of analysing the plausibility of different Nu parameterisations is to compare their predicted offset-temperatures τ_w with values obtained from measurements (Fig. 5d). Here, the possible conclusions are also limited due to the large uncertainties of the water temperature measurements. However, we can at least exclude the Sommers and Rajaram (2020) parameterisation since the corresponding τ_w value lies outside of the 95% interval of the measurements. In our case, sensible heat advection dominates heat from frictional dissipation (Fig. S3), thus it is not surprising that this parameterisation – which is based on a case where frictional dissipation is the only heat source – is not applicable. For the other parameterisations, a clear statement is difficult albeit the parameterisations from the high heat-transfer group are closer to the mean of the measurements and thus likely more appropriate. They contain the parameterisations that are based on field studies (Vincent and others, 2010; Ogier and others, 2021), which could be a motivation for further field experiments specifically targeted to quantify heat transfer.

To summarise, we cannot ascertain the full picture as to why the inferred temperature gradients differ from the melting point gradient and why the one for 21-Aug/AM13 is below and the one for 9-Aug/AM15 above the melting point gradient. To gain more insight, future experiments in artificial moulins would need temperature measurements with higher accuracy, and they could involve several test-sections to get spatially resolved melt rates and temperature gradients. Such spatially resolved measurements would allow to constrain z_{eq} and thus, using Eqn (13), also the Nu parameterisation. More accurate temperature measurements, at an accuracy of ~0.01 °C (compared to 0.05 °C in this study), would allow to discriminate between the two groups of heat-transfer parameterisations (Table 3) using Eqn (11). Hence, it would be possible to calculate Nu and infer its parameterisation in two independent fashions, similar to the approach by Ogier and others (2021).

Summary and outlook

We found that the hydraulic friction factor of the investigated englacial R-channels is not well constrained and that it evolves substantially over the course of a few days. Modelling the evolution of the channel cross-sectional area showed that the simpler channel model by Röthlisberger (1972), which assumes that the water temperature follows the pressure melting point, cannot fully explain observations. However, it is sufficiently accurate to model the size evolution of R-channels in cases where the entry water temperature is close to the melting point.

The investigation of different parameterisations for the Nusselt number was inconclusive but showed that slightly more accurate temperature measurements or several test-sections would have allowed discriminating between them. However, since the uncertainties in the Nusselt number would probably remain considerable, using a range of the Nusselt number values in modelling studies would be prudent. The same consideration applies for the friction factor. In general, this study does not give rise to major concerns about the models that are used today in englacial and subglacial hydrology. However, we suggest that the modelling should follow a more stochastic approach (e.g. Brinkerhoff and others, 2021; Irarrazaval and others, 2021) instead of choosing a single, best-fitting value for each poorly constrained model parameter.

The potential of artificial moulins does not only lie within the investigation of the drainage in englacial R-channels or moulin-like features. We envision them to be useful also for the study of the subglacial drainage system when combined with glacier-wide tracer experiments as the latter have been shown to be significantly impacted by the flow processes within the injection moulin (Schuler and others, 2004; Werder and others, 2010). Characterising the discharge and flow speeds within the moulin using the methods described here would thus allow to partition the effects of subglacial and englacial flow in the corresponding glacier-wide tracer experiments. Moreover, accompanying such tracer experiments with novel autonomous sensing platforms such as the Cryoegg (Prior-Jones and others, 2021), the Glacsweb wireless probe (Hart and others, 2019) or drifters (Alexander and others, 2020) would greatly enhance the scientific yield. Their deployment using artificial moulins would also ensure that these sensing platforms readily reach the subglacial system, without getting stuck or being destroyed on impact when traversing step pool sequences of natural moulins.

Supplementary material. The supplementary material for this article can be found at https://doi.org/10.1017/jog.2022.4.

Data/code availability. The raw data, the code to process the raw data and to produce the results are available at ETHZ Research Collection with DOI https://doi.org/10.3929/ethz-b-000504661.

Acknowledgements. We thank Manuela Köpfli, Jonas Junker, Liz Bagshaw, Mike Prior-Jones, Ludovic Räss, Sebastian Vionnet, Johannes Landmann, Loris Compagno and Julia Schmale for their help with the fieldwork and Sharman Jones for proofreading. We thank Lauren Andrews and an anonymous reviewer for their helpful comments, and Matthew Siegfried for the editing work. The project was co-funded by ETH Zurich, Grant ETH-11 19-2. The salary of D.G. was financed via ETH Grant ETH-661 06 16-2.

References

Alexander A, and 5 others (2020) Pressure and inertia sensing drifters for glacial hydrology flow path measurements. *The Cryosphere* **14**(3), 1009–1023. doi: 10.5194/tc-14-1009-2020

Alley R, Lawson D, Larson G, Evenson E and Baker G (2003) Stabilizing feedbacks in glacier-bed erosion. *Nature* **424**(6950), 758–760. doi: 10.1038/nature01839

Ancey C, and 5 others (2019) Hydraulic reconstruction of the 1818 Giétro glacial lake outburst flood. *Water Resources Research* **55**(11), 8840–8863. doi: 10.1029/2019WR025274

Andrews LC, and 7 others (2014) Direct observations of evolving subglacial drainage beneath the Greenland Ice Sheet. *Nature* **514**(7520), 80–83. doi: 10.1038/nature13796

Bagge Carlson F (2020) MonteCarloMeasurements.jl: Nonlinear Propagation of Arbitrary Multivariate Distributions by means of Method Overloading. ArXiv [preprint], arXiv:2001.07625, https://github.com/baggepinnen/MonteCarloMeasurements.jl v0.10.3.

Bayes F (1958) An essay towards solving a problem in the doctrine of chances. *Biometrika* **45**(3–4), 296–315. doi: 10.1093/biomet/45.3-4.296

Brinkerhoff D, Aschwanden A and Fahnestock M (2021) Constraining subglacial processes from surface velocity observations using surrogate-based Bayesian inference. *Journal of Glaciology* **67**(263), 385–403. doi: 10.1017/jog.2020.112

Bushuk M, Holland DM, Stanton TP, Stern A and Gray C (2019) Ice scallops: a laboratory investigation of the ice–water interface. *Journal of Fluid Mechanics* **873**, 942–976. doi: 10.1017/jfm.2019.398

Chen Y, Liu X, Gulley JD and Mankoff KD (2018) Subglacial conduit roughness: insights from computational fluid dynamics models. *Geophysical Research Letters* **45**(20), 11206–12118. doi: 10.1029/2018GL079590

Church G, and 5 others (2019) Detecting and characterising an englacial conduit network within a temperate Swiss glacier using active seismic, ground penetrating radar and borehole analysis. *Annals of Glaciology* **60**(79), 193–205. doi: 10.1017/aog.2019.19

Church G, Bauder A, Grab M and Maurer H (2021) Ground-penetrating radar imaging reveals glacier's drainage network in 3D. *The Cryosphere* **15**(8), 3975–3988. doi: 10.5194/tc-15-3975-2021

Clarke GKC (2003) Hydraulics of subglacial outburst floods: new insights from the Spring–Hutter formulation. *Journal of Glaciology* **49**(165), 299–313. doi: 10.3189/172756503781830728

Covington MD, Gulley JD, Trunz C, Mejia J and Gadd W (2020) Moulin volumes regulate subglacial water pressure on the Greenland Ice Sheet.

Geophysical Research Letters **47**(20), e2020GL088901. doi: 10.1029/2020GL088901

Cowton T, and 7 others (2013) Evolution of drainage system morphology at a land-terminating Greenlandic outlet glacier. *Journal of Geophysical Research* **118**(1), 29–41. doi: 10.1029/2012JF002540

Dalban Canassy P, Röösli C and Walter F (2016) Seasonal variations of glacier seismicity at the tongue of Rhonegletscher (Switzerland) with a focus on basal icequakes. *Journal of Glaciology* **62**(231), 18–30. doi: 10.1017/jog.2016.3

De Fleurian B, and 9 others (2018) SHMIP the subglacial hydrology model intercomparison project. *Journal of Glaciology* **64**(248), 897–916. doi: 10.1017/jog.2018.78

Egli PE, Irving J and Lane SN (2021) Characterization of subglacial marginal channels using 3-D analysis of high-density ground-penetrating radar data. *Journal of Glaciology* **67**(264), 759–772. doi: 10.1017/jog.2021.26

Flowers GE (2015) Modelling water flow under glaciers and ice sheets. *Proceedings of the Royal Society A: Mathematical, Physical and Engineering Sciences* **471**(2176), 20140907. doi: 10.1098/rspa.2014.0907

Fountain AG (1994) Borehole water-level variations and implications for the subglacial hydraulics of South Cascade Glacier, Washington State, U.S.A. *Journal of Glaciology* **40**(135), 293–304. doi: 10.3189/S0022143000007383

Fountain AG, Jacobel RW, Schlichting R and Jansson P (2005) Fractures as the main pathways of water flow in temperate glaciers. *Nature* **433**(7026), 618–621. doi: 10.1038/nature03296

Gimbert F, Tsai VC, Amundson JM, Bartholomaus TC and Walter JI (2016) Subseasonal changes observed in subglacial channel pressure, size, and sediment transport. *Geophysical Research Letters* **43**(8), 3786–3794. doi: 10.1002/2016GL068337

GLAMOS (1881–2020) Die Gletscher der Schweizer Alpen, 1880–2018/19. Jahrbuch 1-140, Expertenkommission für Kryosphärenmessnetze der Akademie der Naturwissenschaften Schweiz (SCNAT) (doi: 10.18752/glrep_series), vollständige bibliographische Angaben in 'Jahrbuch der Expertenkommission für Kryosphärenmessnetze (SCNAT)', herausgegeben seit 1964 durch die Versuchsanstalt für Wasserbau, Hydrologie und Glaziologie (VAW) der ETH Zürich.

Gnielinski V (1975) Neue Gleichungen für den Wärme- und den Stoffübergang in turbulent durchströmten Rohren und Kanälen. *Forschung im Ingenieurwesen A* **41**(1), 8–16. doi: 10.1007/BF02559682

Goodman J and Weare J (2010) Ensemble samplers with affine invariance. *Communications in Applied Mathematics and Computational Science* **5**(1), 65–80. doi: 10.2140/camcos.2010.5.65

Grab M, and 9 others (2021) Ice thickness distribution of all Swiss glaciers based on extended ground-penetrating radar data and glaciological modeling. *Journal of Glaciology* **67**(266), 1074–1092. doi: 10.1017/jog.2021.55

Gulley JD, and 5 others (2014) Large values of hydraulic roughness in subglacial conduits during conduit enlargement: implications for modeling conduit evolution. *Earth Surface Processes and Landforms* **39**(3), 296–310. doi: 10.1002/esp.3447

Harper JT, Bradford JH, Humphrey NF and Meierbachtol TW (2010) Vertical extension of the subglacial drainage system into basal crevasses. *Nature* **467**(7315), 579–582. doi: 10.1038/nature09398

Harper JT, Humphrey NF and Greenwood MC (2002) Basal conditions and glacier motion during the winter/spring transition, Worthington Glacier, Alaska, USA. *Journal of Glaciology* **48**(160), 42–50. doi: 10.3189/172756502781831629

Harrison WD (1975) Temperature measurements in a temperate glacier. *Journal of Glaciology* **14**(70), 23–30. doi: 10.3189/S0022143000013356

Hart JK, and 5 others (2019) Surface melt driven summer diurnal and winter multi-day stick-slip motion and till sedimentology. *Nature Communications* **10**(1), 1–11. doi: 10.1038/s41467-019-09547-6

Hock R, Iken A and Wangler A (1999) Tracer experiments and borehole observations in the overdeepening of Aletschgletscher, Switzerland. *Annals of Glaciology* **28**, 253–260. doi: 10.3189/172756499781821742

Holmlund P (1988) Internal geometry and evolution of moulins, Storglaciären, Sweden. *Journal of Glaciology* **34**(117), 242–248. doi: 10.3189/S0022143000032305

Hooke RL (1991) Positive feedbacks associated with erosion of glacial cirques and overdeepenings. *Geological Society of America Bulletin* **103**(8), 1104–1108. doi: 10.1130/0016-7606(1991)103<1104:PFAWEO>2.3.CO;2

Hooke RL, Laumann T and Kohler J (1990) Subglacial water pressures and the shape of subglacial conduits. *Journal of Glaciology* **36**(122), 67–71. doi: 10.3189/S0022143000005566

Hubbard B, Sharp M, Willis IC, Nielsen MK and Smart CC (1995) Borehole water-level variations and the structure of the subglacial hydrological system of Haut Glacier d'Arolla, Valais, Switzerland. *Journal of Glaciology* **41**(139), 572–583. doi: 10.1017/s0022143000034894

Huss M, Bauder A, Werder M, Funk M and Hock R (2007) Glacier-dammed lake outburst events of Gornersee, Switzerland. *Journal of Glaciology* **53** (181), 189–200. doi: 10.3189/172756507782202784

Iken A (1972) Measurements of water pressure in moulins as part of a movement study of the White Glacier, Axel Heiberg Island, Northwest Territories, Canada. *Journal of Glaciology* **11**(61), 53–58. doi: 10.3189/S0022143000022486

Iken A, Röthlisberger H and Hutter K (1976) Deep drilling with a hot water jet. *Zeitschrift für Gletscherkunde und Glazialgeologie* **XII**(2), 143–156. doi: 10.1016/0148-9062(79)90440-6

Irarrazaval I, Werder MA, Huss M, Herman F and Mariethoz G (2021) Determining the evolution of an alpine glacier drainage system by solving inverse problems. *Journal of Glaciology* **67**(263), 421–434. doi: 10.1017/jog.2020.116

Isenko E, Naruse R and Mavlyudov B (2005) Water temperature in englacial and supraglacial channels: change along the flow and contribution to ice melting on the channel wall. *Cold Regions Science and Technology* **42**(1), 53–62. doi: 10.1016/j.coldregions.2004.12.003

Landmann JM, and 5 others (2021) Assimilating near real-time mass balance observations into a model ensemble using a particle filter. *The Cryosphere* **15**(11), 5017–5040. doi: 10.5194/tc-15-5017-2021

Linsbauer A, and 7 others (2021) The new Swiss Glacier Inventory SGI2016: from a topographical to a glaciological dataset. *Frontiers in Earth Science* **9**, 704189. doi: 10.3389/feart.2021.704189.

Lunardini VJ, Zisson J and Yen YC (1986) *Experimental determination of heat transfer coefficients in water flowing over a horizontal ice sheet*, Report 86-3. US Army Corps of Engineers, Cold Regions Research & Engineering Laboratory.

Mankoff KD, and 7 others (2017) Roughness of a subglacial conduit under Hansbreen, Svalbard. *Journal of Glaciology* **63**(239), 423–435. doi: 10.1017/jog.2016.134

Nanni U, and 6 others (2020) Quantification of seasonal and diurnal dynamics of subglacial channels using seismic observations on an alpine glacier. *The Cryosphere* **14**(5), 1475–1496. doi: 10.5194/tc-14-1475-2020

Nienow PW, Sharp M and Willis IC (1998) Seasonal changes in the morphology of the subglacial drainage system, Haut Glacier d'Arolla, Switzerland. *Earth Surface Processes and Landforms* **23**(9), 825–843. doi: 10.1002/(sici)1096-9837(199809)23:9<825::aid-esp893>3.0.co;2-2

Nye JF (1976) Water flow in glaciers: jökulhlaups, tunnels and veins. *Journal of Glaciology* **17**(76), 181–207. doi: 10.3189/s002214300001354x

Ogier C, and 6 others (2021) Drainage of an ice-dammed lake through a supraglacial stream: hydraulics and thermodynamics. *The Cryosphere* **15** (11), 5133–5150. doi: 10.5194/tc-15-5133-2021

Prior-Jones MR, and 9 others (2021) Cryoegg: development and field trials of a wireless subglacial probe for deep, fast-moving ice. *Journal of Glaciology* **67**(264), 627–640. doi: 10.1017/jog.2021.16

Röösli C, Walter F, Ampuero JP and Kissling E (2016) Seismic moulin tremor. *Journal of Geophysical Research: Solid Earth* **121**(8), 5838–5858. doi: 10.1002/2015JB012786

Röthlisberger H (1972) Water pressure in intra- and subglacial channels. *Journal of Glaciology* **11**(62), 177–203. doi: 10.1017/cbo9780511667015.003

Röthlisberger H, Iken A and Spring U (1979) Piezometric observations of water pressure at the bed of Swiss glaciers. *Journal of Glaciology* **23**(89), 429–430. doi: 10.3189/S0022143000030197

Schroeder DM, Blankenship DD and Young DA (2013) Evidence for a water system transition beneath Thwaites Glacier, West Antarctica. *Proceedings of the National Academy of Sciences* **110**(30), 12225–12228. doi: 10.1073/pnas.1302828110

Schuler T, Fischer UH and Gudmundsson GH (2004) Diurnal variability of subglacial drainage conditions as revealed by tracer experiments. *Journal of Geophysical Research* **109**(F2), F02008. doi: 10.1029/2003JF000082

Sharp MJ, and others (1993) Geometry, bed topography and drainage system structure of the Haut Glacier d'Arolla, Switzerland. *Earth Surface Processes and Landforms* **18**(6), 557–571. doi: 10.1002/esp.3290180608

Sommers AN and Rajaram H (2020) Energy transfer by turbulent dissipation in glacial conduits. *Journal of Geophysical Research: Earth Surface* **125**(10), e2019JF005502. doi: 10.1029/2019JF005502.

Spring U and Hutter K (1982) Conduit flow of a fluid through its solid phase and its application to intraglacial channel flow. *International Journal of Engineering Sciences* **20**(2), 327–363. doi: 10.1016/0020-7225(82)90029-5

https://doi.org/10.1017/jog.2022.4 Published online by Cambridge University Press

Vincent C, Auclair S and Meur EL (2010) Outburst flood hazard for glacier-dammed lac de Rochemolon, France. *Journal of Glaciology* **56**(195), 91–100. doi: 10.3189/002214310791190857

Weisbach JL (1845) *Lehrbuch der Ingenieur-und Maschinen-Mechanik: Theoretische Mechanik*. Vol. **1**, Druck und Verlag von Friedrich Vieweg und Sohn: Braunschweig.

Werder MA (2016) The hydrology of subglacial overdeepenings: a new supercooling threshold formula. *Geophysical Research Letters* **43**(5), 2045–2052. doi: 10.1002/2015GL067542), 2015GL067542

Werder MA (2021) KissMCMC.jl. https://github.com/mauro3/KissMCMC.jl, v0.2.1.

Werder MA, Hewitt IJ, Schoof CG and Flowers GE (2013) Modeling channelized and distributed subglacial drainage in two dimensions. *Journal of Geophysical Research: Earth Surface* **118**(4), 2140–2158. doi: 10.1002/jgrf.20146

Werder MA, Schuler TV and Funk M (2010) Short term variations of tracer transit speed on alpine glaciers. *The Cryosphere* **4**(3), 381–396. doi: 10.5194/tcd-4-663-2010

https://doi.org/10.1017/jog.2022.4 Published online by Cambridge University Press